TECHNICAL  
REPORTS: DATA

10.1002/2016WR019344

## Key Points:

- A Coastline Resolution Improvement filter is derived to reduce leakage errors across land/ocean boundaries
- A global set of gain factors is derived to reduce leakage errors for continental hydrology applications
- Leakage error reductions are greatest (up to 1–2 cm equivalent water height) for small river basins

## Correspondence to:

D. N. Wiese,  
david.n.wiese@jpl.nasa.gov

## Citation:

Wiese, D. N., F. W. Landerer, and M. M. Watkins (2016), Quantifying and reducing leakage errors in the JPL RL05M GRACE mascon solution, *Water Resour. Res.*, 52, doi:10.1002/2016WR019344.

Received 9 JUN 2016

Accepted 5 SEP 2016

Accepted article online 12 SEP 2016

© 2016. American Geophysical Union.  
All Rights Reserved.

California Institute of Technology.  
Government sponsorship acknowledged.

Quantifying and reducing leakage errors in the JPL RL05M  
GRACE mascon solutionDavid N. Wiese<sup>1</sup>, Felix W. Landerer<sup>1</sup>, and Michael M. Watkins<sup>1</sup><sup>1</sup>Jet Propulsion Laboratory, California Institute of Technology, Pasadena, California, USA

**Abstract** Recent advances in processing data from the Gravity Recovery and Climate Experiment (GRACE) have led to a new generation of gravity solutions constrained within a Bayesian framework to remove correlated errors rather than relying on empirical filters. The JPL RL05M mascon solution is one such solution, solving for mass variations using spherical cap mass concentration elements (mascons), while relying on external information provided by near-global geophysical models to constrain the solution. This new gravity solution is fundamentally different than the traditional spherical harmonic gravity solution, and as such, requires different care when postprocessing. Here we discuss two classes of postprocessing considerations for the JPL RL05M GRACE mascon solution: (1) reducing leakage errors across land/ocean boundaries, and (2) scaling the solutions to account for leakage errors introduced through parameterizing the gravity solution in terms of mascons. A Coastline Resolution Improvement (CRI) filter is developed to reduce leakage errors across coastlines. Synthetic simulations reveal a reduction in leakage errors of ~50%, such that residual leakage errors are ~1 cm equivalent water height (EWH) averaged globally. A set of gain factors is derived to reduce leakage errors for continental hydrology applications. The combined effect of the CRI filter coupled with application of the gain factors, is shown to reduce leakage errors when determining the mass balance of large (>160,000 km<sup>2</sup>) hydrological basins from 11% to 30% (0.6–1.5 mm EWH) averaged globally, with local improvements up to 38%–81% (9–19 mm EWH).

## 1. Introduction

The Gravity Recovery and Climate Experiment (GRACE) has been mapping the spatiotemporal changes of the Earth's surface mass distribution since its launch in 2002 [Tapley *et al.*, 2004a]. This unique data set has allowed for quantification of previously unknown geophysical processes such as continental rates of ice mass changes in Greenland and Antarctica [Luthcke *et al.*, 2013; Shepherd *et al.*, 2012; Velicogna, 2009], rates of groundwater depletion in water-stressed regions across the globe [Richey *et al.*, 2015; Famiglietti *et al.*, 2011; Rodell *et al.*, 2009], unraveling terms in the sea level budget [Reager *et al.*, 2016; Lovel *et al.*, 2014; Boening *et al.*, 2012] and temporal changes in ocean circulation [Landerer *et al.*, 2015]. While GRACE data have proven to be invaluable in understanding and addressing a diverse range of Earth system science related questions, one of the largest shortcomings with the data is the presence of correlated error that manifests itself as North-South stripes due to poor observability of the East-West component of the gravity gradient. Many filters exist to remove this correlated error [Duan *et al.*, 2009] (most of which are empirical by nature), the most common of which includes a form of destriping [Swenson and Wahr, 2006], and smoothing [Wahr *et al.*, 1998]. While these filters are typically successful in removing the correlated error, they have also been shown to remove real geophysical signals from the data which mimic the North-South striping pattern of the error. To compensate for this, a global set of gain factors (limited to continental hydrology applications) has been developed [Landerer and Swenson, 2012] to restore signal amplitudes which were removed in the filtering process. However, these gain factors can potentially introduce biases in frequency bands outside the annual component, in particular for longer-term trends. In those cases, kernel-specific gain factors are necessary [Landerer and Swenson, 2012].

As an alternative to empirical postprocessing filters for removing correlated errors, the gravity solution can be conditioned in such a way that the correlated error is suppressed during the data inversion, effectively eliminating the need for postprocessing. This solution strategy has the unique advantage of allowing the filter to simultaneously adjust all estimated parameters, including not only the basis functions which define the Earth's gravity field, but also the satellite state, accelerometer biases and scale factors, as well as any additional nuisance parameters. Several groups have attempted this, both with spherical harmonic basis functions [Bruinsma

*et al.*, 2010; *Save et al.*, 2012], as well as mascon basis functions [Luthcke *et al.*, 2013; Watkins *et al.*, 2015]. Using mascon basis functions arguably provides a more convenient architecture in which the regularization matrix can be derived, since mascon basis functions are local, rather than global, by nature. This manuscript is focused on the newly released JPL RL05M GRACE mascon solution [Wiese *et al.*, 2015], which is unique in that it uses a near-global set of geophysical models coupled with ancillary remote sensing observations to condition the solution within a Bayesian framework with the purpose of suppressing correlated error during the gravity inversion [Watkins *et al.*, 2015]. The solution is expressed in terms of 4551 equal-area 3° spherical cap mass concentration elements (mascons). This solution has been shown to have distinct advantages over traditional spherical harmonic gravity solutions, including better spatial resolution and more optimal removal of correlated error, in particular for ocean applications [Watkins *et al.*, 2015; Landerer *et al.*, 2015].

While the JPL RL05M mascon solution does not require postprocessing to remove correlated error, we describe in the following two unique postprocessing algorithms that can be applied to the solution to improve local estimates of mass flux by reducing leakage errors intrinsic to the mascon basis functions. Both postprocessing procedures are unique to the JPL RL05M mascon solution and are not directly applicable to other GRACE mascon solutions. The reason for this is that JPL RL05M is currently the only available mascon solution that parameterizes the gravity field in terms of equal-area 3° spherical cap mascons. Other available mascon solutions parameterize the gravity field in terms of a finite spherical harmonic expansion of 1° mascon elements [Luthcke *et al.*, 2013]. Theoretically, the postprocessing algorithms we derive are applicable to mascon elements of any size; however, considering the native GRACE spatial resolution of ~300 km, 1° mascon solutions will have leakage errors that are fundamentally different than those considered here.

This paper is organized in the following manner. First, we describe an algorithm termed the Coastline Resolution Improvement (CRI) filter, which reduces leakage errors across land/ocean boundaries (section 2.1). Second, we describe a global set of gain factors for continental hydrology applications which are derived to compensate for the averaging of the 3° spherical cap mass elements (section 2.2). Finally, a synthetic simulation is performed and the performance of both postprocessing algorithms is quantified (section 3). A CRI-filtered version of the JPL RL05M solution along with the derived gain factors can be found on the GRACE Tellus website ([www.grace.jpl.nasa.gov](http://www.grace.jpl.nasa.gov)) [Wiese *et al.*, 2015].

## 2. Methods

Two distinct postprocessing algorithms are derived which allow for improved spatial resolution of mass flux signals in the JPL RL05M mascon solution via a reduction of leakage errors. Each algorithm is described in this section.

### 2.1. Reducing Leakage Errors Across Coastlines

The JPL RL05M mascon solution solves for monthly gravity anomalies in terms of 4551 equal-area 3° spherical cap mascons, the geophysical placement of which is seen in Figure 1. Note that even though the basis

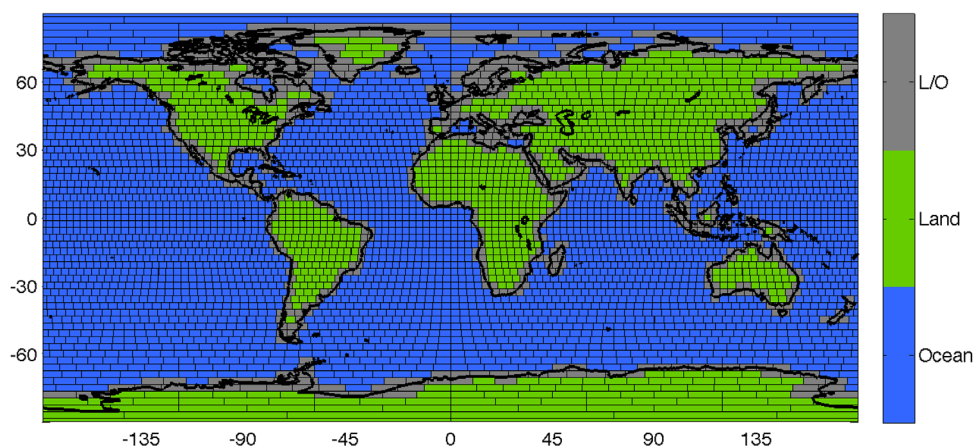


Figure 1. Definition of land, ocean, and land/ocean (L/O) mascons in the JPL RL05M solution.

function consists of spherical caps, each mascon element is represented graphically in Figure 1 as a quadrilateral in order to remove gaps between each spherical cap mascon. The mass within each spherical cap is distributed over the larger area encompassed by the bounding quadrilateral in a mass conserving manner, as discussed in *Watkins et al.* [2015]. Each individual mascon is classified as either “land,” “ocean,” or “land/ocean (L/O)”; 751 of the 4551 mascons are classified as L/O mascons, representing approximately 17% of the population. Here we derive an algorithm to discriminate between the “land” and “ocean” mass portions of each L/O mascon in an attempt to reduce leakage errors across coastlines. This Coastline Resolution Improvement (CRI) correction ultimately allows users to apply an exact averaging kernel when calculating mass flux in hydrological basins near continental boundaries.

The CRI filter is implemented by solving the observation equation

$$H_T A_T = H_L A_L + H_O A_O, \quad (1)$$

where  $H_T$  is the observed total water column height of a specific L/O mascon, and  $H_L$  and  $H_O$  represent the parameters we wish to solve for: the water column height of the land and ocean portions of the L/O mascon, respectively. Furthermore,  $A_T$  represents the total area of the L/O mascon while  $A_L$  and  $A_O$  represent the area of the land and ocean portions, respectively. Equation (1) effectively represents volume conservation within a single mascon.

Equation (1) represents an underdetermined system as the number of unknowns ( $H_L$  and  $H_O$ ) exceeds the number of observations ( $H_T$ ). Therefore, we supplement the system with external a priori information, and solve using batch weighted least squares [*Tapley et al.*, 2004b], formulated in equation (2).

$$(H^T W H + \bar{P}_o^{-1}) \hat{x}_o = H^T W y + \bar{P}_o^{-1} \bar{x}_o \quad (2)$$

In equation (2),  $H$  is a matrix of partial derivatives relating the observations ( $y$ ) to the state parameters ( $\hat{x}_o$ ),  $W$  is a weighting factor on the observation, and  $\bar{x}_o$  is an a priori estimate of the state while  $\bar{P}_o$  contains variance information for  $\bar{x}_o$ .

This problem is relatively straightforward, and we further specify

$$\hat{x}_o = \begin{pmatrix} H_L \\ H_O \end{pmatrix}; \bar{x}_o = \begin{pmatrix} \bar{x}_L \\ \bar{x}_O \end{pmatrix}; \bar{P}_o = \begin{pmatrix} \sigma_L^2 & 0 \\ 0 & \sigma_O^2 \end{pmatrix}; y = H_T; W = \frac{1}{\sigma_{obs}^2} \quad (3)$$

Here  $\bar{x}_L$  and  $\bar{x}_O$  are the a priori estimates for  $H_L$  and  $H_O$ , respectively, while  $\sigma_L$  and  $\sigma_O$  represent a priori variance information for  $\bar{x}_L$  and  $\bar{x}_O$ .  $\sigma_{obs}$  represents uncertainty information on the observation,  $H_T$ , and is specified to be small to force mass conservation during the estimation process.

The critical step in this process is selecting reasonable values for  $\bar{x}_L$ ,  $\bar{x}_O$ ,  $\sigma_L$ , and  $\sigma_O$ . For a given mascon  $i$ ,  $\bar{x}_L^i$  is chosen such that it is the average water column height (area weighted) of all nearby “land” mascons (from  $j=1 \dots N_L$ ) within a radius  $D$  of the L/O mascon in question (equation (4)). Similarly,  $\bar{x}_O^i$  is chosen such that it is the average water column height (area weighted) of all nearby “ocean” mascons (from  $k=1 \dots N_O$ ) within a radius  $D$  of the mascon (equation (5)). We have empirically chosen  $D = 640$  km; this value allows for only nearby mascons to affect the calculation of  $\bar{x}_L$  and  $\bar{x}_O$ . Several values of  $D$  were tested, and we found results to not be overly sensitive to this choice; this is expected so long as there is consistency in the calculation of  $\bar{x}_L$ ,  $\bar{x}_O$ ,  $\sigma_L$ , and  $\sigma_O$ .

$$\bar{x}_L^i = \sum_{j=1}^{N_L} \frac{H_L^j A_L^j}{\sum_{j=1}^{N_L} A_L^j} \Bigg|_{D=640 \text{ km}} \quad (4)$$

$$\bar{x}_O^i = \sum_{k=1}^{N_O} \frac{H_O^k A_O^k}{\sum_{k=1}^{N_O} A_O^k} \Bigg|_{D=640 \text{ km}} \quad (5)$$

The uncertainties on the a priori estimates for a given mascon  $i$  ( $\sigma_L^i$  and  $\sigma_O^i$ ) are then calculated using a time series (from  $t=1 \dots N_t$ ) of both the Global Land Data Assimilation System (GLDAS) land surface hydrology model NOAH [*Rodell et al.*, 2004] and the Estimating the Circulation and Climate of the Ocean, Phase 2

(ECCO2) ocean model [Menemenlis et al., 2008], both represented at 1° spatial resolution. For example, to calculate  $\sigma_L^i$ , we first average the GLDAS model into equal-area 3° mascons consistent with the mascon placement seen in Figure 1. We then calculate the water column height of the land portion of the L/O mascon in question ( $\bar{x}_L^{GLDAS}$ ; this is equivalent to  $H_L$  in equation (3)), and compare this with the average water column height of adjacent land mascons ( $\bar{x}_L^{GLDAS}$ ) within a radius  $D$ , calculated using equation (4). The RMS difference of these two time series (equation (6)) then provides model-derived statistical uncertainty information consistent with the calculation of  $\bar{x}_L^i$  in equation (4). The same process is used to calculate  $\sigma_O^i$ , only the ECCO2 model is used instead of the GLDAS model (equation (7)).

$$\sigma_L^i = \sqrt{\frac{\sum_{t=1}^{N_t} (\bar{x}_L^{GLDAS} - \bar{x}_L^{GLDAS})^2}{N_t}} \quad (6)$$

$$\sigma_O^i = \sqrt{\frac{\sum_{t=1}^{N_t} (\bar{x}_O^{ECCO2} - \bar{x}_O^{ECCO2})^2}{N_t}} \quad (7)$$

This process allows us to provide reasonable a priori estimates for the “land” and “ocean” portions of each L/O mascon globally (equations (4) and (5)) along with model-based statistical variance information on these a priori estimates (equations (6) and (7)), enabling the solution of equation (2). While this process is relatively straightforward, there are a number of issues which require detailed attention. These are addressed in the following subsections.

### 2.1.1. Solid Earth Mass Changes

The CRI filter is designed to accommodate changes in water mass; thus, the effect of solid Earth mass changes must first be removed from the GRACE data prior to implementation. Two such processes which must be accounted for are glacial isostatic adjustment (GIA) and earthquakes. GIA is removed using the model by *A et al.* [2013]; this choice was made to ensure consistency with global gridded data products derived from spherical harmonic solutions currently available on the GRACE Tellus website ([www.grace.jpl.nasa.gov](http://www.grace.jpl.nasa.gov)). Using a different GIA model can change the estimate of water mass for select L/O mascons, which will subsequently change the separation of mass performed by the CRI filter. The GIA sensitivities are well documented, with the greatest uncertainty being in Antarctica [Shepherd et al., 2012].

Earthquake models provided by *Han et al.* [2013] are used to identify mascons that are affected by the coseismic response of the three large earthquakes that have occurred during the GRACE record: the 2004 Sumatra-Andaman earthquake, the 2010 Maule, Chile earthquake, and the 2011 Tohoku-Oki earthquake. Since no comprehensive model is currently available to correct for postseismic relaxation of these earthquakes, we only implement the CRI filter for earthquake-affected mascons prior to the epoch of the earthquake, since any separation of mass after the earthquake would be plagued by uncertainty in the solid Earth postseismic response which we currently cannot account for. These mascons represent a very small fraction of the total percentage of all L/O mascons.

### 2.1.2. Ice-Covered Regions

Ice sheet models are undergoing rapid development, but are currently still limited in reproducing accurate mass changes over the Greenland and Antarctic ice sheets (primarily due to difficulties in modeling ice dynamics). Therefore, these models are likely too uncertain to derive  $\sigma_L$  for these regions. We know, however, that mass fluxes along the coastlines of Greenland and Antarctica (due to glacial dynamics primarily) are larger than neighboring ocean dynamic signals [Chambers, 2009]. Thus, it is desirable in these regions to empirically set  $\sigma_L$  large relative to  $\sigma_O$ . This effectively constrains the estimate of  $H_O$  to be equal to  $\bar{x}_O$ , and the residual mass within the mascon to being placed on the ice sheet. Similarly, this is also done for land-based glaciers with observed large mass trends (i.e., Alaska, Patagonia, Baffin Island, Ellesmere Island, Iceland, and Svalbard).

### 2.1.3. Iteration

Not all L/O mascons have adjacent “land” and “ocean” mascons that can be used to calculate  $\bar{x}_L$ ,  $\bar{x}_O$ ,  $\sigma_L$ , and  $\sigma_O$ . In many instances, the only adjacent mascons (within a radius  $D = 640$  km) are also L/O mascons. In those cases, we invoke an iterative scheme where on the first iteration, only mascons with adjacent “land” and “ocean” mascons are corrected. In all, 52% of the L/O mascons are corrected on this first iteration. On the second iteration, we use the calculated values of  $H_L$  and  $H_O$  from the first iteration to subsequently

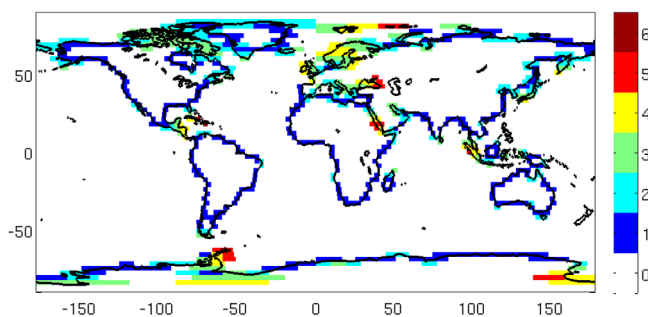


Figure 2. Number of iterations required for the CRI filter.

calculate  $\bar{x}_L$ ,  $\bar{x}_O$ ,  $\sigma_L$ , and  $\sigma_O$  for any remaining L/O mascons. After the second iteration, 79% of all L/O mascons have been corrected. This process repeats until all L/O mascons have been corrected, which for the current mascon grid requires six iterations. The corrections for mascons that require a greater number of iterations (see Figure 2) likely have higher uncertainties, as errors propagate and accumulate in the iterations. For example, the mass balance for the

Black Sea or Red Sea (where mascons require a large number of iterations) will have additional uncertainty in the estimates.

### 2.2. Improving Estimates of Mass Flux at Sub-mascon Resolution

Unconstrained spherical harmonic GRACE solutions require postprocessing filters (typically destriping [Swenson and Wahr, 2006] and/or Gaussian smoothing [Wahr et al., 1998]) to remove correlated errors and reveal geophysical signals. These filters have proven effective in removing correlated North-South errors in the gravity solutions; however, they also have the undesirable effect of removing real geophysical signal, particularly when it is oriented in the North-South direction. This signal can be largely restored through the application of gridded gain factors [Landerer and Swenson, 2012]. These gain factors are derived by implementing the GRACE postprocessing filters on synthetic model data, and performing a least squares fit between the original and postprocessed synthetic data. This provides a direct scaling proportional to the amount of signal damping which is inflicted by the postprocessing procedures. While the gain factors have proven to be effective, they have some regional and time scale dependent limitations, and can be limited in their application to long-term groundwater changes [Landerer and Swenson, 2012].

The concept of applying gain factors to the data is now extended to the JPL RL05M mascon solution. Solving for gravity anomalies in terms of equal-area  $3^\circ$  spherical cap mascons acts as an inherent smoothing function on the true gravity signal, damping power at spatial scales smaller than about  $3^\circ$  (Figure 3). We derive a set of global gain factors for continental hydrology applications to restore this power at short wavelengths. This is performed using a similar technique as outlined in Landerer and Swenson [2012], by first mascon averaging (i.e., performing an area-weighted averaging of mass within the boundaries of each mascon) a land surface hydrology model (we use the Community Land Model (CLM) [Lawrence et al., 2011] at

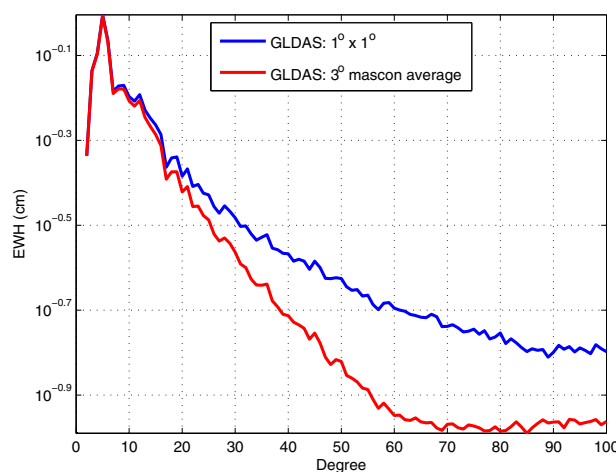
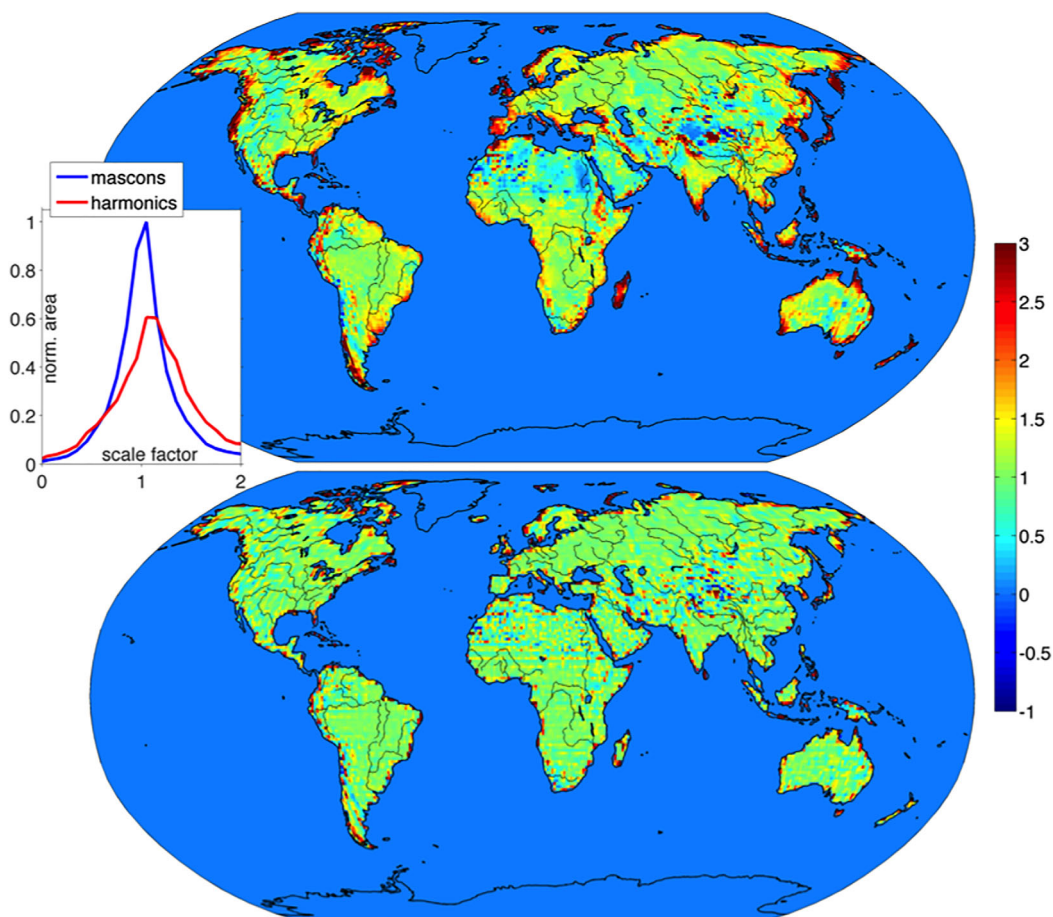


Figure 3. Power as a function of spherical harmonic degree for the  $1^\circ \times 1^\circ$  GLDAS gridded model compared with the power in the model after mascon-averaging.

$1^\circ \times 1^\circ$  resolution) with mascon placements matching the JPL RL05M solution, and then performing a least squares fit between the original model values and the mascon-averaged representation of the model. Since mascon boundaries lie on parallels of  $0.5^\circ$ , the CLM model is first downsampled to  $0.5^\circ \times 0.5^\circ$  prior to performing the least squares fit. This results in a global set of  $0.5^\circ \times 0.5^\circ$  gain factors for continental hydrology applications which redistributes mass within each  $3^\circ$  mascon according to spatial distribution of mass (primarily dominated by the annual cycle) in the land surface hydrology model. Similar to the CRI filter, application of the gain factors directly enables users to apply exact averaging kernels (neglecting the geophysical placement of



**Figure 4.** Gain factors for (top) spherical harmonics solutions based on destriping, smoothing at 300 km, and truncation at spherical harmonic degree 60, and (bottom) JPL RL05M mascon solutions based on 3° mascon averaging. The inset histogram shows the distribution of gain factors for each approach.

mascon boundaries) when analyzing mass flux in hydrological basins, effectively reducing leakage errors introduced by the mascon basis function. However, as in *Landerer and Swenson* [2012], we emphasize that this downscaling does not imply that mass changes at the gain-factor resolution are now independently resolved. Rather, all sub-mascon grid points are still correlated (i.e., no phase changes introduced), though amplitudes can vary.

The resulting map of gain factors is shown in Figure 4, and is compared with gain factors derived for the spherical harmonic solutions as described in *Landerer and Swenson* [2012]. The mascon gain factors are largest in regions with large spatial gradients in mass distribution at short length scales, such as along coastlines and in High Mountain Asia. Notably, the gain factors for the mascons are significantly smaller and closer to 1 than for the harmonic solutions. This indicates that the final mass flux solutions are less sensitive to the derived gain factor. A gain factor closer to unity also reduces the potential for biasing long-term signals in cases where the gain factors are mostly driven by annual signals.

The gain factors must be applied after the implementation of the CRI-filter, not before. Additionally, we note that the gain factors should not be used in regions where the CLM model is unreliable or incomplete (i.e., ice mass variations which are poorly modeled in CLM, or near inland seas). In this analysis, gain factors are not computed over ice-covered regions, primarily because accurate models depicting estimates of ice mass balance (including surface mass balance processes coupled with ice dynamics) still lack maturity. Furthermore, gain factors over the ocean are not considered as monthly ocean bottom pressure variations, especially in the deeper ocean, are mostly characterized by length scales larger than 500–1000 km on monthly and longer time scales [*Chambers and Bonin*, 2012].

### 3. Synthetic Simulation and Results

To quantify the performance of the CRI filter in reducing leakage errors across land/ocean boundaries along with the utility of the application of hydrology gain factors, we create a synthetic simulation. Global monthly surface mass variations are created by adding together the CLM (Lawrence *et al.*, 2011) (hydrology) and OMCT (Dobslaw *et al.*, 2013) (ocean) models from January 2005 to December 2009 at  $1^\circ \times 1^\circ$  resolution. Additionally, over Greenland and Antarctica, we add the ice component of the European Space Agency (ESA) Earth System Model (ESM<sub>ice</sub>) [Dobslaw *et al.*, 2015], which uses two configurations of the Regional Atmospheric Climate Model (RACMO) [Ettema *et al.*, 2009] to model surface mass balance processes while simultaneously accounting for secular trends due to ice dynamics in locations where observed surface velocities exceed 50 m/yr. We use a  $1^\circ \times 1^\circ$  gridded representation of monthly averages of a spherical harmonic expansion to degree and order 180 of ESM<sub>ice</sub>. ESM<sub>ice</sub> is available for 1996–2006; hence, we use January 2002 to December 2006 in our simulation, adding it to CLM and OMCT from January 2005 to December 2009. The discrepancy in timeframe between the models should have negligible impact on the results of the simulation, as the parameterization of the CRI filter is self-contained to strictly land or ocean regions, and does not rely on coupling between the two. Note that glaciers not on Greenland or Antarctica are excluded from the composite model, as they are not modeled in CLM, and not fully represented in ESM<sub>ice</sub>. This composite model (GLDAS + OMCT + ESM<sub>ice</sub>) is then mascon averaged to emulate the spatial sampling of the JPL RL05M GRACE solution. We then apply the CRI filter to the composite model to separate land and ocean mass from mascons that span coastlines. Since the a priori variance information in the CRI filter is derived from the GLDAS (hydrology) and ECCO2 (ocean) models (ref equations (6) and (7)), the parameterization of the CRI filter is sufficiently independent of the synthetic simulation (in the sense that different forward models are employed). We do note, however, that using CLM instead of GLDAS in equation (6) to parameterize the CRI filter does not change the results substantially, as the relative ratio of  $\sigma_L^i$  to  $\sigma_O^i$  is fairly constant independent of which land surface hydrology model is used.

Figure 5 shows the magnitude of the monthly error RMS over all L/O mascons separately for regions with and without ice, for both ocean leakage errors (i.e., errors over the ocean) and land leakage errors (i.e., errors over the land). The relative magnitude of ocean and land leakage errors is primarily a function of how the mascon placement conforms to the coastline (i.e., whether there are more ocean or land pixels within each L/O mascon). The magnitude of the monthly leakage error is typically between 1.5 and 2 cm equivalent water height (EWH) for non-ice-covered regions, and reaches up to 10 cm EWH for ice-covered regions. After the CRI filter is implemented, the leakage error is reduced to around 1 cm EWH in most months for non-ice-covered regions, and between 1 and 2 cm EWH for ice-covered regions. It is also interesting to note that the error after implementing the CRI filter scales proportionally to the magnitude of the original error; Figure 5 shows a slight positive trend in the error both before and after implementation of the CRI filter for both regions. This occurs as larger spatial

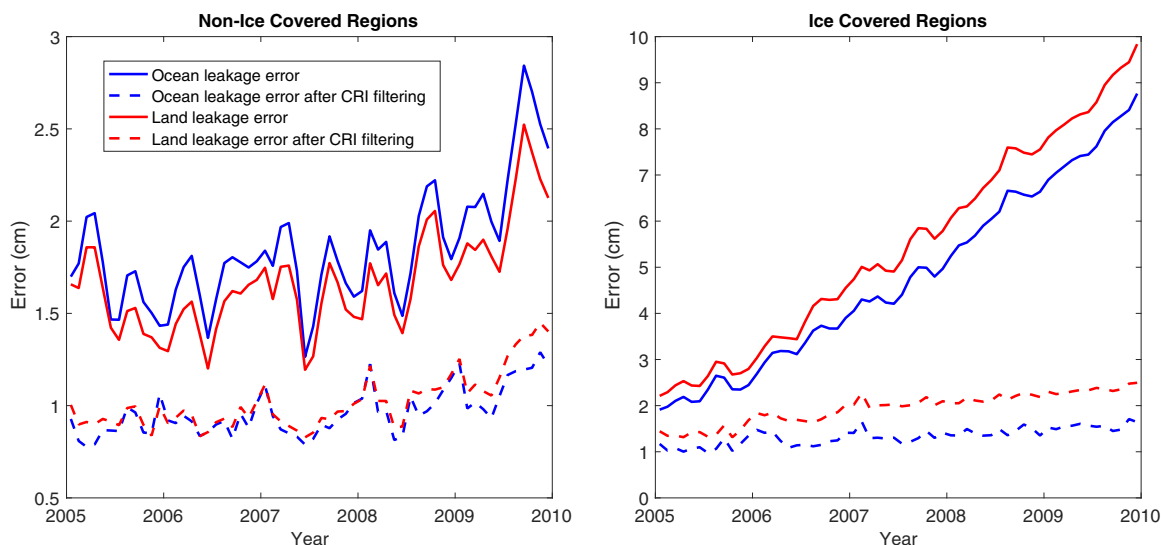


**Figure 5.** Monthly error RMS of all L/O mascons for (left) non-ice-covered regions and (right) ice-covered regions, for ocean leakage errors (errors over the ocean) and land leakage errors (errors over the land) both before and after implementation of the CRI filter.

gradients in mass across coastlines lead to larger differences between  $\bar{x}_O$  and  $\bar{x}_L$  with fixed values for  $\sigma_L$  and  $\sigma_O$ , allowing the magnitude of the spatial gradient in mass to be proportional to the error in the filter. The increase in the magnitude of the spatial gradient in mass across coastlines through time is attributed to trends in CLM near coastlines for the non-ice-covered regions, and to secular trends in ice dynamics in outlet glaciers for ice-covered regions. An examination of errors spatially reveals that largest errors are present in mascons with highly skewed ratios of land and ocean area within an individual L/O mascon. The CRI filter performs poorly in these mascons, and this is especially the case in ice-covered regions since  $\sigma_L$  is empirically set to be large (section 2.1.2).

**Table 1.** Hydrological Basins (Listed in Order of Decreasing Size) and Associated Error RMS in Determining Mass Variations Within Each Basin Over the 5 Year Synthetic Simulation Which Uses the CLM and OMCT Models as the *truth*<sup>a</sup>

Basin Name	$\mathcal{E}_{MSCN}^m$	$\mathcal{E}_{MSCN}^l$	$\mathcal{E}_{CRI}^{l,r}$	$\mathcal{E}_{CRI,GF,CLM}^{l,r}$	$\mathcal{E}_{CRI,GF,GLDAS}^{l,r}$
1) Amazon	6.1	1.5	1.3	0.9	1.8
2) Nile	4.0	1.5	1.2	0.8	1.0
3) Zaire	5.3	2.7	2.8	2.7	3.0
4) Mississippi	4.6	1.3	1.2	1.0	1.2
5) Ob	3.2	0.6	0.6	0.5	0.5
6) Parana	6.4	3.2	3.2	1.7	2.8
7) Yenisei	3.8	0.6	0.6	0.6	0.7
8) Lena	3.2	1.2	1.0	0.9	0.7
9) Niger	4.7	1.6	1.6	1.4	1.5
10) ChangJiang	5.6	2.4	2.3	2.1	2.4
11) Amur	4.7	2.4	1.8	1.3	1.6
12) Mackenzie	5.6	2.0	2.1	1.6	1.8
13) Ganges	8.0	2.5	2.5	2.9	3.1
14) Volga	5.3	1.9	1.9	1.4	1.8
15) Zambezi	8.9	2.8	2.6	2.5	2.7
16) Indus	6.5	6.6	6.6	4.3	5.5
17) Nelson	6.9	5.9	6.0	4.7	5.9
18) St. Lawrence	7.9	1.8	1.8	1.9	1.7
19) Orinoco	13.4	5.2	4.7	3.1	3.9
20) Murray	6.5	2.0	1.7	1.5	1.8
21) ShattelArab	7.1	1.1	1.1	1.2	1.2
22) Orange	5.2	2.6	2.7	1.9	2.4
23) HuangHe	6.1	3.2	3.2	3.2	2.9
24) Yukon	5.8	3.5	4.4	2.9	4.3
25) Senegal	5.0	4.2	4.5	1.4	2.3
26) Jubba	7.0	2.8	2.4	1.6	1.8
27) Colorado(Arizona)	5.8	2.2	2.3	1.9	2.2
28) RioGrande(US)	6.7	1.9	2.0	1.1	1.5
29) Danube	7.9	5.7	4.4	3.6	4.3
30) Tocantins	14.8	3.7	3.7	3.8	3.8
31) Mekong	17.0	10.0	7.0	5.9	7.5
32) Columbia	9.8	3.4	2.5	2.4	3.4
33) Kolyma	5.6	3.9	2.0	1.3	1.6
34) SaoFrancisco	11.6	5.6	5.5	5.8	6.1
35) Dnepr	8.9	2.5	2.4	2.3	2.2
36) Don	9.7	7.2	6.6	5.1	5.2
37) Colorado(Argentina)	12.8	7.2	7.1	6.8	9.6
38) Irrawaddy	22.0	23.6	21.7	16.1	19.4
39) Volta	11.6	7.8	6.7	4.5	5.5
40) Khatanga	5.7	3.3	3.3	3.3	3.8
41) Dvina	8.5	3.4	3.2	3.1	3.3
42) Indigirka	4.9	3.5	3.9	3.5	3.6
43) Pechora	8.7	6.1	2.9	2.7	3.6
44) Ural	8.3	4.3	4.3	3.4	3.5
45) Salween	11.9	15.2	15.1	13.6	17.3
46) Magdalena	19.2	17.9	15.0	11.5	14.4
47) Fraser	17.5	10.9	11.8	9.0	15.3
48) Anadyr	9.5	7.1	5.9	4.8	4.9
49) Yana	6.9	5.9	6.0	5.7	7.9
50) Olenek	6.5	3.6	3.2	3.2	3.3
51) Taz	10.4	6.2	6.2	3.2	3.1
52) Sacramento-San Joaquin	13.7	23.5	13.9	4.5	14.5
Mean	8.3	5.1	4.5	3.5	4.4

<sup>a</sup> $\mathcal{E}_{MSCN}^m$  is the GRACE measurement error,  $\mathcal{E}_{MSCN}^l$  is the leakage error introduced by the choice of basis function, i.e., by mascon-averaging,  $\mathcal{E}_{CRI}^{l,r}$  is the residual leakage error after implementing the CRI filter,  $\mathcal{E}_{CRI,GF,CLM}^{l,r}$  is the residual leakage error after implementing the CRI filter and applying gain factors derived from the CLM model, and  $\mathcal{E}_{CRI,GF,GLDAS}^{l,r}$  is the residual leakage error after implementing the CRI filter and applying gain factors derived from the GLDAS model. Results are provided in terms of absolute error in units of millimeter of equivalent water height.

coastlines for the non-ice-covered regions, and to secular trends in ice dynamics in outlet glaciers for ice-covered regions. An examination of errors spatially reveals that largest errors are present in mascons with highly skewed ratios of land and ocean area within an individual L/O mascon. The CRI filter performs poorly in these mascons, and this is especially the case in ice-covered regions since  $\sigma_L$  is empirically set to be large (section 2.1.2).

Table 1 and Figure 6 summarize results from the simulation in recovering mass in 52 of the world's largest hydrological basins. For each basin, we provide estimates of measurement error ( $\mathcal{E}_{MSCN}^m$ ), leakage error ( $\mathcal{E}_{MSCN}^l$ ), and residual leakage error ( $\mathcal{E}^{l,r}$ ). Residual leakage errors quantify remaining leakage error after applying one or more of the post-processing algorithms described in this paper. The measurement error (Table 1, column 2; Figure 6, blue bars) is calculated using the scaled (by a factor 2) diagonal elements of the formal covariance matrix from the GRACE JPL RLO5M gravity solution [Wiese et al., 2015]. The scale factor of 2 is regarded to provide a conservative estimate of uncertainty, as resulting estimates are approximately the same order of magnitude as errors estimated using techniques outlined by Wahr et al. [2006]. In Wahr et al. [2006], errors are estimated by examining residuals of the GRACE estimate of mass over a basin with respect to a fit of a mathematical function (typically a linear as well as a sinusoid with a period of 1 year) to the data. These residuals represent both GRACE measurement error as well as interannual geophysical signal; as such, this approach

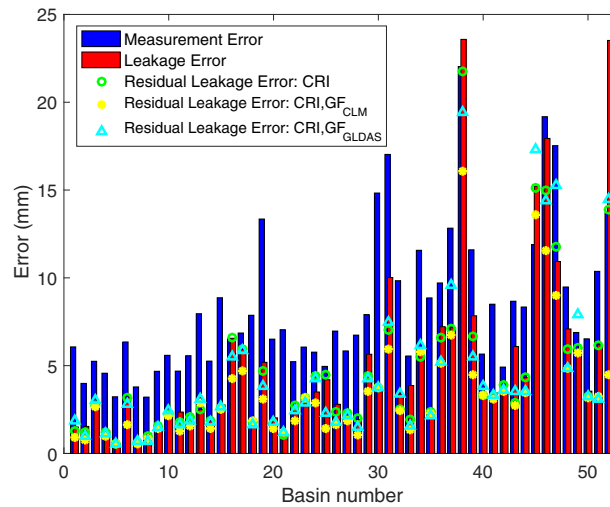


**Figure 6.** Error budget for 52 of the world's largest hydrological basins in order of decreasing size (refer to Table 1 for corresponding basin names) showing the measurement error (blue bars), leakage error (red bars), and residual leakage errors after (1) CRI filtering (green circles), (2) CRI filtering and applying gain factors derived from CLM (yellow stars), and (3) CRI filtering and applying gain factors derived from GLDAS (cyan triangles).

these basins have a greater percentage of their area composed of partial mascons. For select basins, leakage errors even eclipse measurement errors (most notably the Salween and Sacramento-San Joaquin basins). Largest leakage errors are found in the Irrawaddy and Sacramento-San Joaquin basins, where an error of 2.4 cm EWH is introduced. However, we note that these basin-specific leakage errors are still substantially smaller than when conventional spherical harmonic postprocessing filters are applied [Landerer and Swenson, 2012].

To the extent that a portion of the hydrological basin lies near coastlines, some of the leakage error can be corrected by implementing the CRI filter. Column 4 in Table 1 and Figure 6 (green circles) show the residual leakage error after implementing the CRI filter ( $\mathcal{E}_{CRI}^{r}$ ), calculated as the monthly error RMS over the 5 year synthetic simulation period. Basins for which the CRI filter has the greatest impact are the Sacramento-San Joaquin, Pechora, Magdalena, and Mekong river basins, reducing leakage errors by 9.6, 3.2, 3.0, and 3.0 mm, respectively. There are several basins where implementing the CRI filter actually increases the overall level

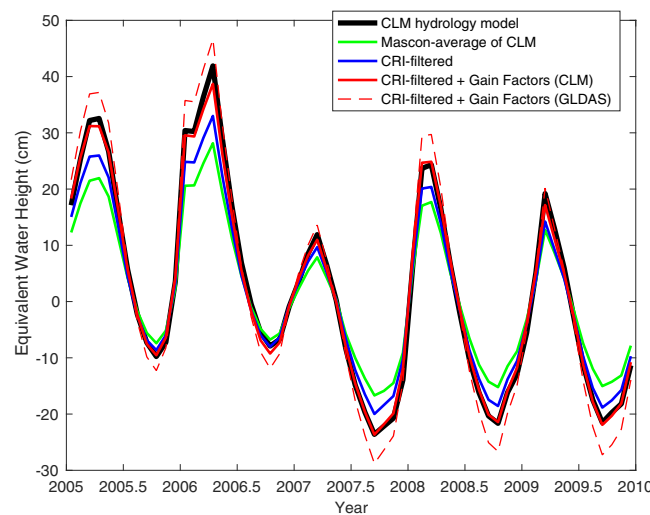


**Figure 7.** Time series of mass in the Sacramento-San Joaquin river basin for the synthetic simulation.

presents a conservative estimate of uncertainty.

Estimates of leakage error (Table 1, column 3; Figure 6, red bars) capture the error that mascon-averaging introduces: provided is the error RMS (over 60 months) between the composite model and the mascon-averaged representation of that model within each basin. The leakage error is primarily a function of how the shape of the basin conforms to the placement of the mascons, convolved with the spatial heterogeneity of mass within mascons that lie on basin boundaries. On average, measurement errors dominate leakage errors (mean error of 8.3 mm versus 5.1 mm); this is particularly the case for larger basins (Figure 6) as the fraction of fully contained mascons in the basins increases. For smaller basins, leakage errors tend to be on par with measurement errors, as

of error rather than reducing it, the largest of which is found in the Yukon and Fraser river basins. Here the error is increased by almost 1 mm with the CRI filter, indicating that the CRI filter is (relatively) ineffective in this region. This is an area where the near-coastal ocean mass is spatially heterogeneous with nearby open ocean regions according to the ECCO2 model. Similarly, for land: according to the GLDAS model, the mass signature near the coastal regions is heterogeneous with respect to neighboring areas further from the coast. In this circumstance, both  $\sigma_L$  and  $\sigma_O$  are large, leaving little statistical information that the filter can rely on to correctly perform the separation of mass.

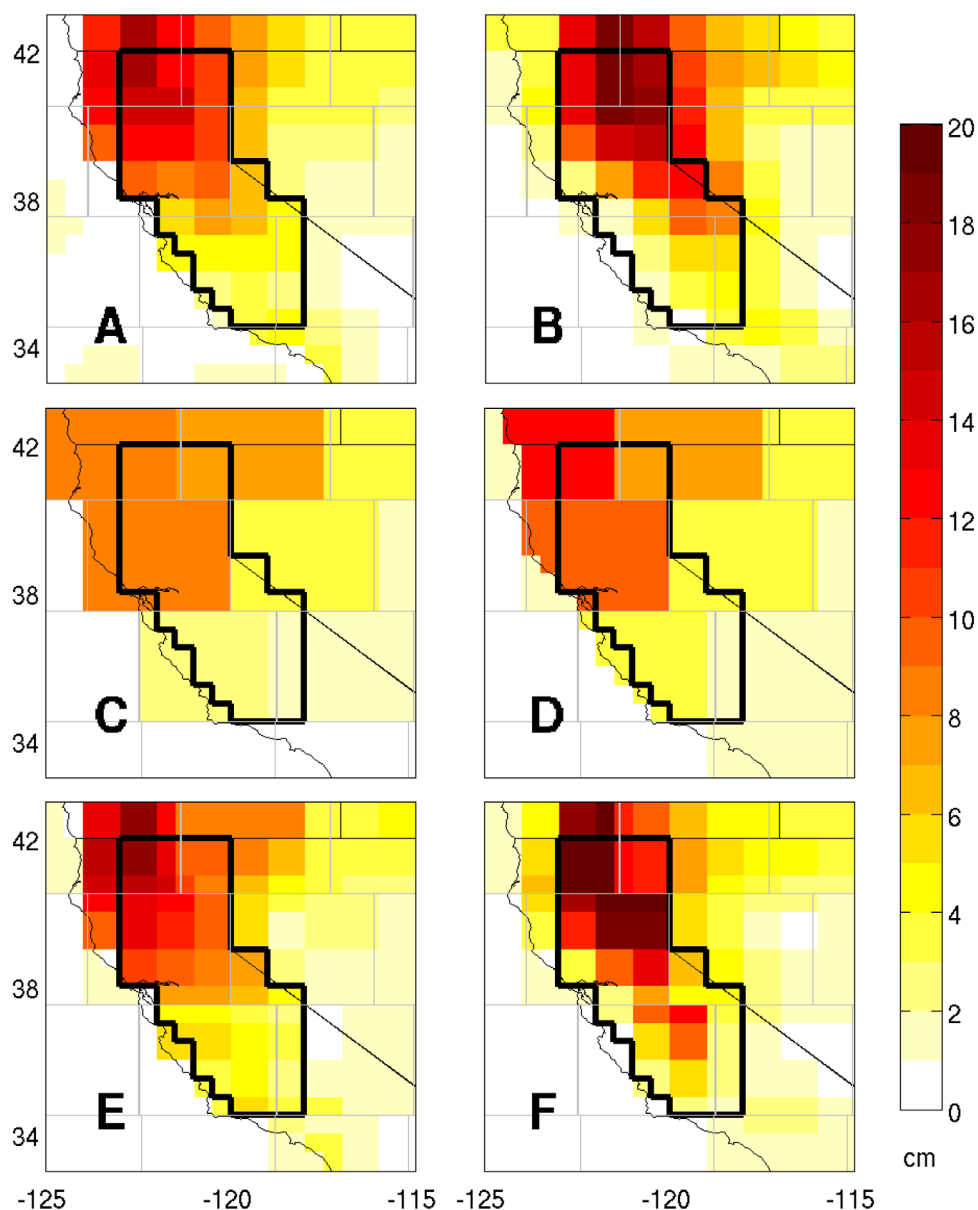


**Figure 8.** The 2005–2009 annual amplitude of (a) CLM + OMCT at  $1^\circ \times 1^\circ$  resolution, (b) GLDAS + ECCO2 at  $1^\circ \times 1^\circ$  resolution, (c) after mascon-averaging the time series in Figure 8a—this represents the native resolution of the mascon basis function, (d) after CRI-filtering Figure 8c, (e) after applying CLM-derived gain factors to Figure 8d, and (f) after applying GLDAS-derived gain factors to Figure 8d. The outline of the Sacramento-San Joaquin river basin is given in dark black, and the outline of the mascon placement is given in light gray.

Columns 5 and 6 in Table 1, along with Figure 6 (yellow stars, cyan triangles), show the residual leakage errors after application of gain factors derived from the CLM hydrology model ( $\mathcal{E}_{CRI,GF_{CLM}}^{l,r}$ ), and the GLDAS hydrology model ( $\mathcal{E}_{CRI,GF_{GLDAS}}^{l,r}$ ), respectively, calculated as the monthly error RMS over the 5 year synthetic simulation period. Since CLM is the *truth* model used in the simulation,  $\mathcal{E}_{CRI,GF_{CLM}}^{l,r}$  is considered to provide an upper bound on the effect of the application of gain factors in reducing leakage errors within each basin. It is seen that for the largest basins, not only does the application of gain factors have a small effect, but the overall result is fairly insensitive to the choice of model used to derive gain factors. The largest sensitivities to the choice of model in deriving gain factors are seen in smaller river basins; for instance, leakage errors are reduced in the Sacramento-San Joaquin River Basin by 19 mm (81%) using CLM-derived gain factors, and only reduced by 9 mm (38%) using GLDAS-derived gain factors. In some instances, leakage errors are increased with the application of gain factors rather than decreased. The most extreme example of this is in the Fraser River Basin, where applying CLM-derived gain factors reduces error by 1.9 mm, but applying

GLDAS-derived gain factors increases error by 4.4 mm. Overall, however, we see that results are fairly insensitive to the choice of model used to derive gain factors: there are only seven river basins where the differences exceed 2 mm RMS, and only 13 basins where the differences exceed 1 mm RMS. These differences are small when compared to the magnitude of the measurement error within each basin (Figure 6). For the basins that do differ the most, the discrepancies highlight the disagreement in the spatial allocation of mass at sub-mascon resolutions within the model domains. On average, we see that the application of the CRI filter and gain factors reduces leakage errors by a modest 0.6–1.5 mm (11%–30%), with much stronger improvements locally (up to 9–19 mm) in small river basins.

As an example of the application of the CRI filter and gain factors, we analyze the recovery of mass within the Sacramento-San Joaquin river basin based on the synthetic simulation (Figures 7 and 8). This is a small river basin ( $\sim 160,000 \text{ km}^2$ ), and has the second highest leakage error of the basins we examined ( $\mathcal{E}_{MSCN}^l$ , Table 1). The river basin is fully contained within six mascons; none of which lie entirely within its domain (Figure 8). This convolution of the geophysical placement of the mascons with the outline of the Sacramento-San Joaquin River Basin leads to a large value for  $\mathcal{E}_{MSCN}^l$ , manifesting as a damping of the annual cycle of recovered mass in the basin time series (Figure 7, green line). The spatial distribution of this mass damping is seen in Figure 8c, in comparison with Figure 8a. The fact that half of the mascons contain mixed land/ocean signals indicate that this basin will be sensitive to the application of the CRI filter. After applying the CRI filter, a significant portion of mass is restored (Figure 7, blue line), and leakage errors are reduced by 40% (Table 1). The spatial distribution of mass after application of the CRI filter is seen in Figure 8d. Finally, application of the CLM-derived gain factors is largely successful in restoring mass from outside the basin boundary to within the basin boundary, reducing leakage errors by 81% (Table 1), while successfully restoring the suppressed annual amplitude (Figure 7, red line). Comparing Figure 8e with Figure 8a reveals that application of the gain factors is successful to a large extent in restoring mass in the correct locations within the river basin boundary, at sub-mascon spatial resolution. The sensitivity to the choice of model used to derive the gain factors is additionally addressed. Figure 8b shows the annual amplitude of mass according to the GLDAS model, which places slightly less mass along the northern coast of California than the CLM model (Figure 8a). Application of gain factors derived from the GLDAS model subsequently results in placing too much mass within the basin boundary (Figure 8f), and not enough along the coasts in this region. This results in an overestimate of the annual cycle (Figure 7, dashed red line), and a slight increase in the overall error RMS relative to only applying the CRI filter and no scaling (Table 1). We note that the Sacramento-San Joaquin basin has the largest sensitivity to the two differing sets of gain factors from the set of hydrological basins we examined, with an RMS difference in mass estimates of 1 cm EWH.

#### 4. Discussion

In this manuscript, we have derived and described in detail two postprocessing algorithms for the JPL RL05M mascon solution. First, a Coastline Resolution Improvement (CRI) filter is derived to separate land and ocean mass within mascons that span coastlines. Globally, this algorithm reduces land/ocean leakage errors in our synthetic simulation for non-ice-covered regions by nearly 50%, from 2 cm equivalent water height to 1 cm equivalent water height. For ice-covered regions, large leakage errors due to mass loss trends in outlet glaciers are effectively reduced by  $\sim 80\%$  at the end of our synthetic simulation: from 10 cm equivalent water height to 2 cm equivalent water height. The CRI filter performs less well in regions with skewed ratios of land to ocean area within a particular L/O mascon; thus, interpreting results within these mascons requires care. The overall general effectiveness of the CRI filter in reducing leakage errors, however, underscores the importance of applying it when studying mass signals near coastal regions using the JPL RL05M GRACE solution.

Second, we derive a set of global grid point gain factors for applications to continental hydrology. These gain factors are designed to redistribute and effectively down-scale mass to sub-mascon spatial scales. These gain factors enable a reduction of leakage error when users apply exact averaging kernels for the calculation of mass flux within specific hydrological basin boundaries (as opposed to averaging along mascon boundaries). In our synthetic simulation, we find that, on average, mass flux estimates in 52 of the world's largest river basins are modestly improved, showing a reduction in leakage errors of 0.6–1.5 mm EWH (11%–30%) with the application of the CRI filter and the gain factors, significantly smaller than the mean GRACE measurement error within the basins (8.3 mm EWH). Local reductions in leakage error for smaller

river basins are more substantial, reaching up to 9–19 mm EWH in the Sacramento-San Joaquin River Basin, the same order of magnitude as the GRACE measurement error within the basin (14 mm EWH). Discrepancies in the spatial distribution of mass within differing land surface hydrology models leads to relatively minor differences in the recovery of mass within each basin, depending upon which model is used to derive gain factors. This difference is less than 1 mm RMS for 39 of the 52 river basins examined, and is consistently smaller than the GRACE measurement error for each basin examined. Differences are most prevalent for smaller river basins, implying that extra care is warranted when quantifying leakage errors within these basins.

Overall, the magnitude of the reduction in leakage errors due to the application of gain factors and the CRI filter is modest in comparison with the reported GRACE measurement error when averaging over large hydrological basins. However, the leakage errors are not Gaussian by nature, but manifest as biases (albeit small) in the GRACE results. Therefore, we recommend application of the CRI filter and gain factors when using the JPL RL05M solution. These corrections will have the largest effects when studying small spatial regions.

### Acknowledgments

The research described in this paper was carried out at the Jet Propulsion Laboratory, California Institute of Technology, under a contract with the National Aeronautics and Space Administration. The JPL RL05M solution with the CRI filter implemented, along with the associated scale factors are available via the Physical Oceanography Distributed Archive Center (PODAAC) as well as the GRACE Tellus websites.

### References

- A, G., J. Wahr, and S. Zhong (2013), Computations of the viscoelastic response of a 3-D compressible Earth to surface loading: an application to Glacial Isostatic Adjustment in Antarctica and Canada, *Geophys. J. Int.*, *192*, 557–572, doi:10.1093/gji/ggs030.
- Boening, C., J. K. Willis, F. W. Landerer, R. S. Nerem, and J. Fasullo (2012), The 2011 La Niña: So strong, the oceans fell, *Geophys. Res. Lett.*, *39*, L19602, doi:10.1029/2012GL053055.
- Bruinsma, S., J. M. Lemoine, R. Biancale, and N. Vales (2010), CNES/GRGS 10-day gravity field models (release 2) and their evaluation, *Adv. Space Res.*, *45*(4), 587–601, doi:10.1016/j.asr.2009.10.012.
- Chambers, D. P. (2009), Calculating trends from GRACE in the presence of large changes in continental ice storage and ocean mass, *Geophys. J. Int.*, *176*(2), 415–419, doi:10.1111/j.1365-246X.2008.04012.x.
- Chambers, D. P., and J. A. Bonin (2012), Evaluation of Release-05 GRACE time-variable gravity coefficients over the ocean, *Ocean Sci.*, *8*, 859–868, doi:10.5194/os-8-859-2012.
- Dobslaw, H., F. Flechtner, I. Bergmann-Wolf, C. Dahle, R. Dill, S. Esselborn, I. Sasgen, and M. Thomas (2013), Simulating high-frequency atmosphere-ocean mass variability for dealiasing of satellite gravity observations: AOD RL05, *J. Geophys. Res. Oceans*, *118*, 3704–3711, doi:10.1002/jgrc.20271.
- Dobslaw, H., I. Bergmann-Wolf, R. Dill, E. Foroootan, V. Klemann, J. Kusche, and I. Sasgen (2015), The updated ESA Earth System Model for future gravity mission simulation studies, *J. Geod.*, *89*, 505–513, doi:10.1007/s00190-014-0787-8.
- Duan, X. J., J. Y. Guo, C. K. Shum, and W. van der Wal (2009), On the postprocessing removal of correlated errors in GRACE temporal gravity field solutions, *J. Geod.*, *83*, 1095, doi:10.1007/s00190-009-0327-0.
- Ettema, J., M. R. van den Broeke, E. van Meijgaard, W. J. van de Berg, J. L. Bamber, J. E. Box, and R. C. Bales (2009), Higher surface mass balance of the Greenland ice-sheet revealed by high-resolution climate modeling, *Geophys. Res. Lett.*, *36*, L12501, doi:10.1029/2009GL038110.
- Famiglietti, J. S., M.-H. Lo, S. L. Ho, J. Bethune, K. J. Anderson, T. H. Syed, S. C. Swenson, C. R. deLinage, and M. Rodell (2011), Satellites measure recent rates of groundwater depletion in California's Central Valley, *Geophys. Res. Lett.*, *38*, L03403, doi:10.1029/2010GL046442.
- Han, S.-C., R. Riva, J. Sauber, and E. Okal (2013), Source parameter inversion for recent great earthquakes from a decade-long observation of global gravity fields, *J. Geophys. Res. Solid Earth*, *118*, 1240–1267, doi:10.1002/jgrb.50116.
- Landerer, F. W., and S. C. Swenson (2012), Accuracy of scaled GRACE terrestrial water storage estimates, *Water Resour. Res.*, *48*, W04531, doi:10.1029/2011WR011453.
- Landerer, F. W., D. N. Wiese, K. Bentel, C. Boening, and M. Watkins (2015), North Atlantic meridional overturning circulation variations from GRACE ocean bottom pressure anomalies, *Geophys. Res. Lett.*, *42*, 8114–8121, doi:10.1002/2015GL065730.
- Lawrence, D. M., et al. (2011), Parameterization improvements and functional and structural advances in version 4 of the Community Land Model, *J. Adv. Model. Earth Syst.*, *3*, M03001, doi:10.1029/2011MS000045.
- Llovel, W., J. K. Willis, F. W. Landerer, and I. Fukumori (2014), Deep-ocean contribution to sea level and energy budget not detectable over the past decade, *Nat. Clim. Change*, *4*, 1031–1035, doi:10.1038/nclimate2387.
- Luthcke, S. B., T. J. Sabaka, B. D. Loomis, A. A. Arendt, J. J. McCarthy, and J. Camp (2013), Antarctica, Greenland, and Gulf of Alaska land-ice evolution from an iterated GRACE global mascon solution, *J. Glaciol.*, *59*(216), 613–631, doi:10.3189/2013JoG12J147.
- Menemenlis, D., J. Campin, P. Heimbach, C. Hill, T. Lee, A. Nguyen, M. Schodlock, and H. Zhang (2008), ECCO2: High resolution global ocean and sea ice data synthesis, *Mercator Ocean Quart. Newsl.*, *31*, 13–21.
- Reager, J. T., A. S. Gardner, J. S. Famiglietti, D. N. Wiese, A. Eicker, and M.-H. Lo (2016), A decade of sea level rise slowed by climate-driven hydrology, *Science*, *351*(6274), 699–703, doi:10.1126/science.aad8386.
- Richey, A. S., B. F. Thomas, M.-H. Lo, J. T. Reager, J. S. Famiglietti, K. Voss, S. Swenson, and M. Rodell (2015), Quantifying renewable groundwater stress with GRACE, *Water Resour. Res.*, *51*, 5217–5238, doi:10.1002/2015WR017349.
- Rodell, M., et al. (2004), The global land data assimilation system, *Bull. Am. Meteorol. Soc.*, *85*, 381–394, doi:10.1175/BAMS-85-3-381.
- Rodell, M., I. Velicogna, and J. Famiglietti (2009), Satellite-based estimates of groundwater depletion in India, *Nature*, *460*, 999–1002, doi:10.1038/nature08238.
- Save, H., S. Bettadpur, and B. D. Tapley (2012), Reducing errors in the GRACE gravity solution using regularization, *J. Geod.*, *86*(9), 695–711, doi:10.1007/s00190-012-0548-5.
- Shepherd, A., et al. (2012), A reconciled estimate of ice-sheet mass balance, *Science*, *338*(6111), 1183–1189, doi:10.1126/science.1228102.
- Swenson, S., and J. Wahr (2006), Post-processing removal of correlated errors in GRACE data, *Geophys. Res. Lett.*, *33*, L08402, doi:10.1029/2005GL025285.
- Tapley, B. D., S. Bettadpur, J. C. Ries, P. F. Thompson, and M. M. Watkins (2004a), GRACE measurements of mass variability in the Earth system, *Science*, *305*(5683), 503–505, doi:10.1126/science.1099192.
- Tapley, B. D., B. E. Schutz, and G. H. Born (2004b), *Statistical Orbit Determination*, Elsevier, San Diego, Calif.

- Velicogna, I. (2009), Increasing rates of ice mass loss from the Greenland and Antarctic ice sheets revealed by GRACE, *Geophys. Res. Lett.*, 36, L19503, doi:10.1029/2009GL040222.
- Wahr, J., M. Molenaar, and F. Bryan (1998), Time variability of the Earth's gravity field: Hydrological and oceanic effects and their possible detection using GRACE, *J. Geophys. Res.*, 103(B12), 30,205–30,229, doi:10.1029/98JB02844.
- Wahr, J., S. Swenson, and I. Velicogna (2006), Accuracy of GRACE mass estimates, *Geophys. Res. Lett.*, 33, L06401, doi:10.1029/2005GL025305.
- Watkins, M. M., D. N. Wiese, D.-N. Yuan, C. Boening, and F. W. Landerer (2015), Improved methods for observing Earth's time variable mass distribution with GRACE using spherical cap mascons, *J. Geophys. Res. Solid Earth*, 120, 2648–2671, doi:10.1002/2014JB011547.
- Wiese, D. N., D.-N. Yuan, C. Boening, F. W. Landerer, and M. M. Watkins (2015), *JPL GRACE Mascon Ocean, Ice, and Hydrology Equivalent Water Height JPL RL05M.1. Ver. 1*, PO.DAAC, Calif., doi:10.5067/TEMSC-OCL05.